Thermo-mechanical simulation of annealing heat treatment of Ni-based GH4099 superalloy made by laser powder bed fusion

Xufei Lu[a,*], Chao Chen[b], Guohao Zhang[c], Michele Chiumenti[a], Miguel Cervera[a], Haoliang Yin[b], Liang Ma[c], Xin Lin[c,*]

[a] *International Centre for Numerical Methods in Engineering, Polytechnical University of Catalonia, Barcelona, Spain*

[b] *ChengDu TongYu Aeronautical Facility Manufacturing Co., Ltd, Chengdu, China*

[c] *State Key Laboratory of Solidification Processing, Northwestern Polytechnical University, Xi'an, China*

Abstract:

Laser powder bed fusion (LPBF) additive manufacturing (AM) unavoidably generates residual stresses due to sharp thermal gradients and the strong mechanical constraints of the substrate. These stresses can lead to large warpages and cracking of AM builds, compromising their qualification. Annealing heat treatment (HT) after LPBF fabrication is an efficient solution for residual stress relaxation, allowing for the development of visco-strains above the annealing temperature. Thereby, this work is focused on the thermo-mechanical simulation of the post-HT of Ni-based GH4099 superalloy components fabricated by LPBF. To this end, several bridge structures are manufactured by LPBF, and various annealing HT conditions are analyzed. After cutting from the substrate, the warpage of all the AM-parts is measured using a 3D-scanner. The in-house software package for the numerical simulation of both the AM and the HT processes first is calibrated by matching the experimental measurements. Next, the numerical tool is used to investigate the effect of different annealing conditions (e.g. varying temperature and dwell time) on the relaxation of the residual stresses and warpage. A roadmap to select the optimal annealing parameters is established considering the actual size of the AM-components.

Key words:

Laser powder bed fusion; Residual stresses relaxation; Annealing heat treatment; Part warpages; Ni-based superalloy; Finite element simulation.

* Corresponding author.

E-mail address: xlu@cimne.upc.edu (X. Lu); xlin@nwpu.edu.cn (X. Lin)

1 Introduction

Additive manufacturing (AM), defined by the ISO/ASTM 52900 standard terminology [1], is an advanced fabrication technique that has been broadly adopted in different industrial sectors such as aerospace, automobile and medicine due to its ability to 3D-print arbitrarily complex components [2]. Laser powder bed fusion (LPBF) is one of the most precise metal AM technologies, where a focused laser beam is used to selectively melt a fine powder bed in a layer-by-layer sequence to build metallic components [3]. During the LPBF process, the intense energy input generates a small melt-pool. The process is characterized by high thermal gradients in the heat affected zone (HAZ). When the thermal expansion or contraction of the metal deposition is prevented by the stiffness of the substrate (or the currently printed component section), either residual stresses or plastic deformations are generated in the AM-build [4-6]. Unfortunately, these residual stresses induce large distortions when the built parts are cut from the substrate, and reduce the mechanical performance and fatigue life of the final products [7-9].

Due to the magnitude of the residual stresses in AM, the key factors responsible for their formation and how to mitigate them are being actively investigated [10-21]. A strategy to reduce residual stresses focuses on the optimization of the process parameters in AM such as the laser power, the scan speed and the scan path. In this line, Zhang et al. [10] found that a ‘dual-laser following but time-delayed’ scan strategy can minimize residual stresses in multi-laser beam powder bed fusion. Promoppatum et al. [11] investigated the influence of the energy input on residual stress reduction and recommended optimal process conditions. Another approach consists of modifying the substrate geometry. Lu et al. [11] reported that the geometrical structure of the substrate can significantly affect the thermal and mechanical response during laser-directed energy deposition. The substrate preheating [13,14] or the use of auxiliary rolling [15] and laser shock peening [16] can also help to mitigate the residual stresses and the part warpage.

Despite these approaches, the eradication of the residual stresses in AM-parts is still a complex task. An alternative to tackle this problem is the post-process heat treatment (HT) [17] applied after the AM buildup and before removing the substrate. During HT, two main mechanisms are responsible for stress relief [18]. On the one hand, when increasing the temperature, the yield strength of the materials decreases. Thus, the accumulated residual stresses exceed the plastic yielding. On the other hand, the material behavior at high temperatures is characterized by large visco-plastic strains (creep), which mitigate the residual stresses.

Therefore, for the qualification of AM components is often required the integration of different processes, e.g. the LPBF fabrication is followed by the HT and the final cutting operations to remove the substrate. However, the analysis of the evolution of both the thermal and mechanical response during the entire manufacturing chain is still challenging.

Taking into account the high cost of the experiments and the urgent need for an optimal HT road map, the computational simulation is regarded as an appealing alternative solution. Focusing on the numerical simulation of the post-HT process after AM fabrication, Baere et al. [22] proposed an Arrhenius-type creep equation to predict the effect of the temperature and the holding time during HT on the stress relief in simple Ti6Al4V cantilever structures made by LPBF. In this work, a process window for post-HT is provided. Cardon et al. [23] employed a thermo-viscoplastic model and conducted different creep tests to investigate how the HT parameters affect the

residual stress field and distortions in LPBF Ti6Al4V components. They found that the hydrostatic pressure is not responsible for the stationary creep rate. Jin et al. [24] developed a finite element (FE) model to predict the annealing behavior of AISI 316L parts fabricated by LPBF, using creep material properties. They validated the model using two different structures (an auxetic cantilever and a propeller) and achieved good prediction accuracy. Williams et al. [25] investigated the impact of post-annealing HT (at 700°C for 2 h) on residual stresses in additively manufactured 316L stainless steel by combining FE analysis with neutron diffraction measurements. Their result showed that peak residual stresses are reduced by around 10% and 40% in the vertical and horizontal samples, respectively. Li et al. [26] developed a FE framework including a precipitate evolution model to analyze the mechanical properties of 6xxx aluminum alloy series printed by LPBF, followed by the HT process. They obtained a hardness increase of 63.1%, compared to the as-built sample when the heat-treatment is realized at 170 °C for 18.8 h. Unfortunately, most of the research work is focused on the metallurgical evolution during the HT [27-30]; the thermo-mechanical response during the post-annealing process requires more effort.

Ni-based superalloys play a significant role in industrial applications. In particular, the GH4099 is a typical precipitation-strengthened Ni-based superalloy that exhibits excellent mechanical properties and thermal stability at elevated temperatures (up to 1000°C); thus, it is a good candidate for many aeronautical applications such as the engine combustion chamber and structural stiffeners [27,28]. With the growing demand for complex high-performance metallic parts in the aeronautical and aerospace sectors, the fabrication by additive manufacturing of Ni-based superalloys has also gained significant attention.

The objectives of this work are the following: (i) to perform the thermomechanical simulation of the entire AM process chain including the LPBF, followed by the annealing HT and the final substrate removal; (ii) to analyze the influence of different HT conditions (i.e. the HT temperature and the dwell time) and the component size on the relaxation of residual stresses; (iii) to yield the optimal HT process window for the qualification of AM-components. To this end, seven bridge structures of Ni-based GH4099 superalloy first are printed using the LPBF technique and then undergo different HT process conditions. The residual warpage of all the bridge structures is measured using a 3D scanner once cut from the substrates. The in-house coupled thermo-mechanical framework for the simulation of the AM process is enhanced to account for the HT analysis. The developed numerical model is calibrated with the generated experimental data. Finally, the validated model is employed to define the optimal HT process window.

2 Experimental procedure

2.1 Materials

In this study, the substrate is an annealed 316L stainless steel plate of 250×250×25 mm^3. In order to remove both oil and the oxide film, the base plate is polished with sandpaper and cleaned using acetone. The powder material is a Ni-based GH4099 superalloy produced by the electrode induction melting inert gas atomization (EIGA) method. The powder diameter ranges between 15~53 μm and its chemical composition is listed in Table 1. Before the LPBF fabrication, the GH4099 powder is dried in a vacuum oven at 120 °C for 2 h to remove the moisture.

Table 1. Chemical compositions of the GH4099 powder used.

Element	Cr	Co	O	W	Ti	Mo	C	Ce	Si	Al	Fe	Mn	Ni
wt.%	18.88	7.15	0.013	6.37	1.38	4.12	0.04	0.012	0.32	2.07	1.22	0.28	Bal.

2.2 LPBF experiment

Seven identical bridge-shaped structures with 39 archway supports are additively manufactured using an EOS M290 LPBF machine with a Yb-fiber laser with a maximum power of 400 W and an argon atmosphere with a low level of oxygen to prevent oxidation. Fig. 1 shows the geometric dimensions of the bridge structure. Because of the large printing job, the base plate can accommodate one part in each fabrication, only; thus, the same LPBF process is repeated seven times.

The process parameters adopted to inform the printing machine are listed in Table 2. The substrate is not preheated. The LPBF process uses an alternating scanning strategy with a rotation angle of 67º. The scanning sequence is a stripe strategy where each island is 10 mm wide with an overlap of 0.02 mm among them.

After the LPBF fabrication, the loose powder is removed. The built structures are kept anchored to the base plate till the end of the HT process.

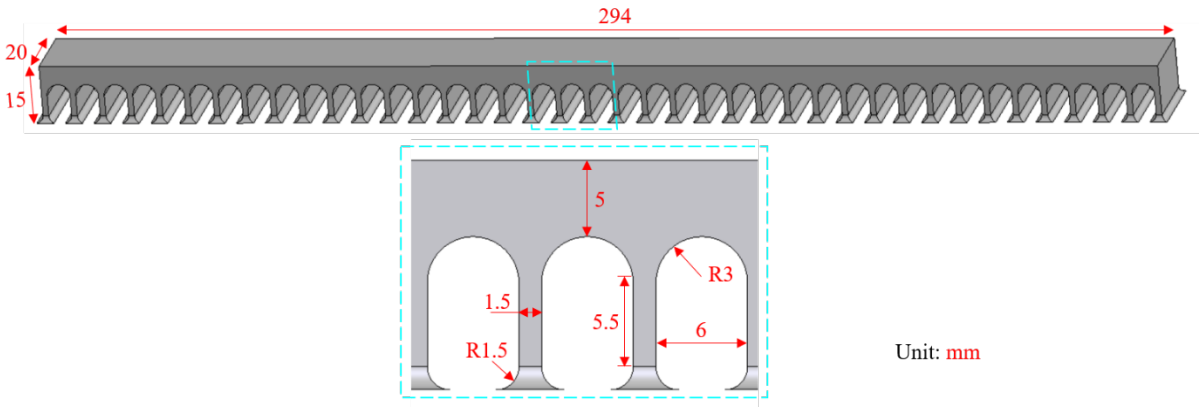

Fig. 1. Geometric dimensions of the bridge component fabricated by LPBF.

Table 2. Building parameters used for the LPBF process.

Laser power (W)	Layer thickness (μm)	Scan speed (mm/s)	Hatch distance (μm)	Laser beam diameter (μm)
300	40	1060	100	100

2.3 Post-annealing HT process

With the same printing operation for all the bridge components, six different annealing HT conditions are applied to analyze their effectiveness in relieving the residual stresses accumulated during the LPBF process. The reference is a printed bridge structure not subjected to the post-HT process. After printing, the rest of the bridge structures are heated to the selected HT temperature with a temperature rate of about 10 °C/min. Different dwell-time settings are applied afterwards. Finally, a cooling rate of 2~5 °C/min is used to reach room temperature. In this work, four different annealing temperatures of 500°C, 600°C, 900°C and 1100°C are adopted. Two different dwell-times of 4 h and 8 h are considered when the annealing temperature is 500°C. Similarly, when the annealing temperature is 1100°C, two different dwell-times of 1 h and 2 h are considered. For the annealing temperatures of 600°C and 900°C, the corresponding dwell-times are set to 2 h and 4 h, respectively. Fig. 2 shows the six diverse HT conditions used.

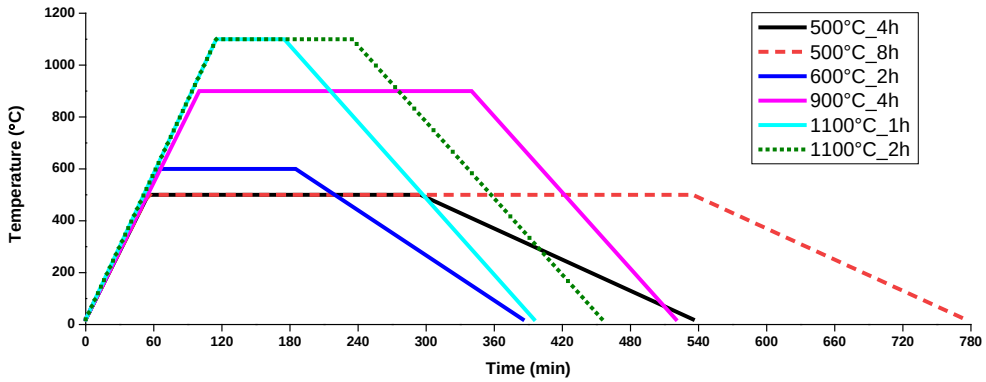

Fig. 2. Six different annealing HT conditions applied to the bridge parts.

2.4 Substrate removal and warpage measurements

After the annealing HT, the substrate is removed by cutting the support legs of the bridge structures by wire electric discharge machining (WEDM). As a consequence, the residual stresses still existing after the annealing process cause the structural warpage, as shown in Fig. 3.

To measure the warpage of all the printed bridge components, a *Breuckmann Smart SCAN3D* scanner with an accuracy of 0.015 mm is employed. The deformed components are compared to the nominal CAD geometry using the *Geomagic Control X* software. In particular, the vertical displacement distribution at the top surface of the bridge structures is recorded for each HT condition.

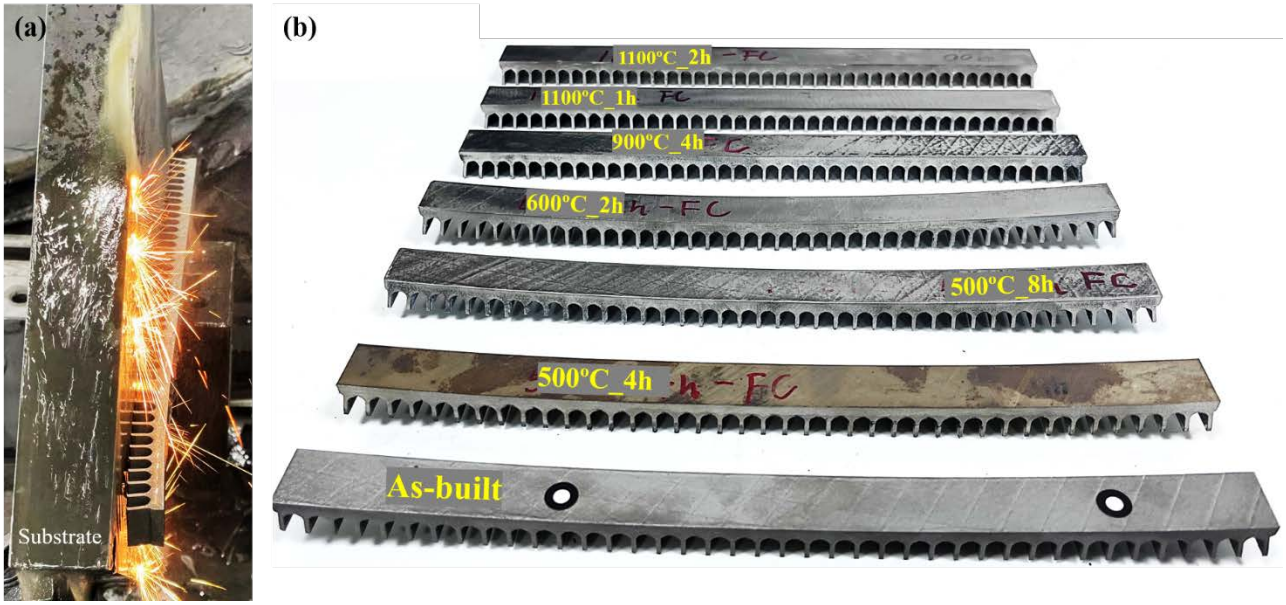

Fig. 3. (a) Substrate removal process through WEDM; (b) Structural warpage after cutting from the base plate.

3 Computational simulation

3.1 FE modeling of LPBF and post-annealing

In this work, the prediction of the thermal and mechanical response of the AM parts during the LPBF process as well as the simulation of the post-HT process are computed using the in-house coupled thermo-mechanical software COMET [31,32]. The thermo-mechanical coupling is tackled by a fractional step method leading to a staggered iterative solution. Therefore, for each time step of the process, the transient heat transfer analysis is

computed first, followed by the stress analysis driven by the resulting temperature field.

The latent heat contribution is neglected because the time-scale of the phase change is much smaller than the time-stepping adopted for the thermal transient analysis.

The metal AM process is simulated by using the *birth-death-element* activation technique. Thus, the elements belonging to the newly deposited layer are activated following the movement of the moving heat source as defined by the scanning strategy [33,34]. An equivalent thermal boundary condition is used to consider the effects of the loose powder bed surrounding the AM-part. Also, the power bed is too loose to affect the mechanical behavior of the builds during the LPBF process; thus, the loose powder is not included in the computational domain. A layer-by-layer activation strategy is adopted, improving the computational efficiency without compromising the required simulation accuracy [35,36].

To simulate the proposed post-annealing conditions, time-dependent Dirichlet boundary conditions are used to prescribe the temperature evolution for all the nodes belonging to the external surfaces of the component, as in the actual experiments. The final WEDM cutting stage is simulated by releasing the existing constraining of the support structures with the base plate.

3.2 Thermomechanical governing equations

During the LPBF processes, the heating and cooling cycles are controlled by the energy balance equation:

$$\dot{H} = -\nabla \cdot \mathbf{q} + \dot{Q} \tag{1}$$

where $\dot{H}$ is the enthalpy rate. The volumetric heat source, $\dot{Q}$, is computed as:

$$\dot{Q} = \frac{\dot{P}\eta}{V_{pool}} \tag{2}$$

where $\dot{P}$ is the nominal laser power, η is the actual power absorption parameter and $V_{pool} = w^2(h_l + h_r)$ is the melt-pool volume being w the laser spot diameter, h_l the thickness of the layer and h_r is the melt-pool depth.

The heat flux, $\mathbf{q}$, is expressed through Fourier's law:

$$\mathbf{q} = -k\nabla T \tag{3}$$

where $k(T)$ and ∇T are the thermal conductivity coefficient and the thermal gradients, respectively.

The heat loss due to convection is defined by Newton's law:

$$q_{conv} = h_{conv}(T - T_{room}) \tag{4}$$

where h_{conv} is the Heat Transfer Coefficient (HTC) by convection, T is the temperature of the part surface and T_{room} is the room temperature.

The radiation heat flux is obtained by Stefan-Boltzmann's law:

$$q_{rad} = \varepsilon_{rad}\sigma_{rad}(T^4 - T_{room}^4) \tag{5}$$

where ε_{rad} is the emissivity coefficient and σ_{rad} is the Stefan Boltzmann constant.

The mechanical problem is governed by the balance of momentum and the continuity equations:

$$\nabla \cdot \mathbf{s} + \nabla p + \mathbf{b} = 0 \tag{6}$$

$$(\nabla \cdot \mathbf{u} - e^T) - \frac{p}{K} = 0 \tag{7}$$

where **b** are the body forces, **u** is the displacement field, e^T is the thermal deformation, $K(T)$ is the bulk (or compressibility) modulus while **s** and p are the spherical and deviatoric parts of the Cauchy stress tensor, $\boldsymbol{\sigma}$:

$$\boldsymbol{\sigma} = p\boldsymbol{I} + \mathbf{s}(\mathbf{u}) \tag{8}$$

3.3 Material constitutive model

The constitutive model characterizes the material behavior in the whole temperature range from room temperature, T_{room} to and above the melting point, T_{melt} and during both the LPBF and post-HT processes; it models elasto-visco-plastic behavior for the solid phase and pure viscous behavior for the mushy and liquid phases, respectively [37]. The smooth transition between the solid and the liquid-like behavior takes place when the annealing temperature, T_{anne} is overpassed. Thermal softening is controlled by a temperature-dependent yield surface which contracts till vanishing at the melting temperature, T_{melt}. Thereby, the solid-to-liquid phase-change is forced by the solid fraction function, $0 \leq f_S(T) \leq 1$ for $T_{anne} \leq T \leq T_{melt}$.

Thus, the mechanical constitutive equations take the form:

$$p = \frac{K}{f_S(T)}(e^{vol} - e^T) \tag{9}$$

$$\mathbf{s} = \frac{2G}{f_S(T)}(\mathbf{e} - \mathbf{e}^{vp}) \tag{10}$$

where $G(T)$ is the temperature-dependent shear modulus, $\mathbf{e}^{vp}$ are the visco-plastic strains, **e** and e^{vol} are the deviatoric and volumetric parts of the total strain tensor, respectively. The thermal deformation, e^T, is computed as:

$$e^T(T, f_S) = e^{cool}(T) + e^{pc}(f_S) \tag{11}$$

where $e^{cool}(T)$ is the thermal expansion/contraction while $e^{pc}(f_S)$ is the thermal shrinkage during the liquid-to-solid phase-change, defined as:

$$e^{cool}(T) = 3[\alpha(T)(T - T_{room}) + \alpha(T_0)(T_0 - T_{room})] \tag{12}$$

$$e^{pc}(f_S) = \beta f_S \tag{13}$$

where T_0 is the initial temperature, taken the same as T_{room}, α and β are the thermal expansion and shrinkage coefficients, respectively.

A temperature-dependent von-Mises yield surface is used:

$$\Phi(\mathbf{s}, q_h, T) = \|\mathbf{s}\| - f_S\sqrt{\frac{2}{3}}\left[\sigma_y(T) - q_h\right] \tag{14}$$

where $\sigma_y(T)$ is the temperature-dependent yield stress while q_h represents the stress-like variable controlling the isotropic strain-hardening, defined as:

$$q_h(\xi, T) = -\left[\sigma_\infty(T) - \sigma_y(T)\right]\left[1 - e^{-\delta(T)\xi}\right] - h(T)\xi \tag{15}$$

where $\sigma_\infty(T)$ is the temperature-dependent saturation flow stress and δ and h are the parameters used to control the exponential and linear hardening laws, respectively.

The (deviatoric) visco-plastic strains, $\boldsymbol{\varepsilon}^{vp} = \mathbf{e}^{vp}$, together with the evolution law of the isotropic strain-hardening variable, ξ, are obtained from the principle of maximum plastic dissipation as:

$$\dot{\mathbf{e}}^{vp} = \dot{\gamma}^{vp}\frac{\partial\Phi(\mathbf{s},q_h,T)}{\partial\mathbf{s}} = \dot{\gamma}^{vp}\frac{\mathbf{s}}{\|\mathbf{s}\|} = \dot{\gamma}^{vp}\mathbf{n} \tag{16}$$

$$\dot{\xi} = \dot{\gamma}^{vp}\frac{\partial\Phi(\mathbf{s},q_h,T)}{\partial q_h} = \sqrt{\frac{2}{3}}\dot{\gamma}^{vp} \tag{17}$$

where $\mathbf{n} = \frac{\partial \Phi(\mathbf{s},q_h,T)}{\partial \mathbf{s}}$ is the normal to the yield surface, and $\dot{\gamma}^{vp}$ is the visco-plastic multiplier, evaluated as:

$$\dot{\gamma}^{vp} = \langle \frac{\Phi(\mathbf{s},q_h,T)}{\eta} \rangle^{\frac{1}{m}} \tag{18}$$

where $\langle \cdot \rangle$ are the Macaulay brackets, while m and η are the rate sensitivity and plastic viscosity, respectively. Note that $\Phi(\mathbf{s}, q_h, T) \to 0$ as the temperature reaches the melting point. Hereafter, viscous behavior is recovered as [38]:

$$\mathbf{s} = \eta (\dot{\gamma}^{vp})^{m-1} \, \dot{\mathbf{e}}^{vp} \tag{19}$$

3.3 FE mesh, material properties and boundary conditions

Fig. 4 shows the CAD geometry of the bridge AM-components used as the mock-up in this work. The figure also shows the corresponding FE meshes consisting of 272,289 Q1P0 hexahedral elements and 226,560 nodes. In this study, 6.25 physical layers are grouped into one multi-layer for the FE simulations to balance the computational cost and the prediction accuracy. The mesh size is set to 0.25×1.25×0.25 mm^3 for the supporting structure and 1.25×1.25×0.25 mm^3 for the upper bench. The effect of the substrate is considered using equivalent thermo-mechanical boundary conditions.

Fig. 4. 3D FE meshes of the bridge part.

The material properties correspond to the GH4099 Ni-based superalloy: the material density and Poisson's ratio are 8470 kg/m^3 and 0.37, respectively. Linear hardening is considered in the constitutive model, and the isotropic strain-hardening variable is set to $\xi = 10$ MPa and the corresponding parameter is $h = 1$. The other temperature-dependent thermophysical properties are represented in Fig. 5 [28,39-41]. The material creep expected at the highest temperatures during the printing process as well as during the post-HT phase depends on the value chosen for the plastic viscosity, η, and the corresponding rate sensitivity, m. The numerical calibration of both parameters is carried out by matching the simulated results to the available experimental data. The result of the calibration is reported in Fig. 5 together with the temperature-dependent yield stress used in the simulation to deal with the thermal softening.

The temperature evolution during the printing process strictly depends on the power input by the laser and the heat loss, mainly due to the heat conduction through the base plate. Thus, the power absorption is set to 45% [42-44] while an equivalent HTC by conduction of 1000 W/(m^2·°C) is considered to account for the heat flux to the

base plate. The heat loss through the upper surface of the builds depends on both heat convection and radiation. The HTC by convection is set to 15 W/(m^2·ºC) with a room temperature of 23ºC while the emissivity of the heat radiation law is set to 0.54 [45,46].

During the mechanical analysis of both the LPBF and the post-annealing process, the bottom of the supporting structures of the bridge part are clamped as in the actual experimental setups. This mechanical constraining is released to model the cutting phase.

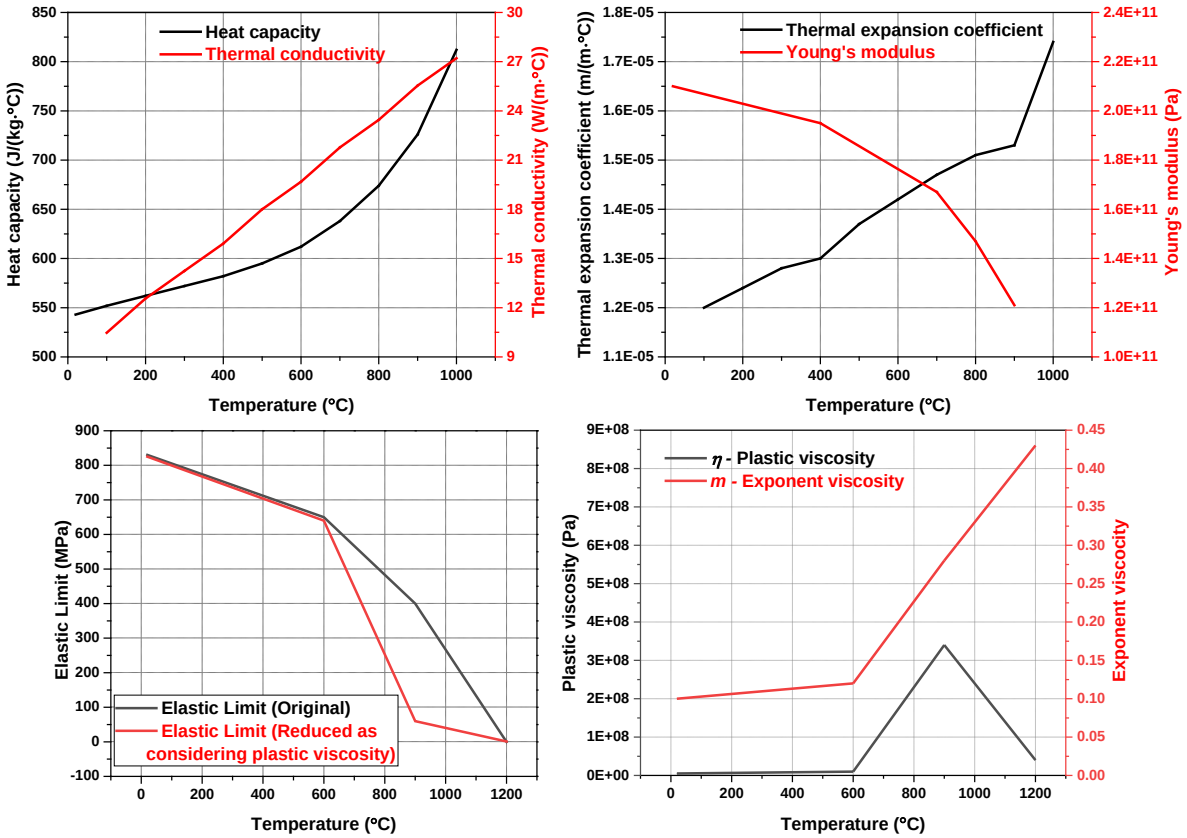

Fig. 5. Temperature-dependent material properties of GH4099 Ni-based superalloy.

4 Results and discussion

4.1 Measured part warpages and model validation

Figs. 6 and 7 show the contour-fills of the vertical (Z-direction) displacement as well as the displacement distribution along the longitudinal direction (mid-section) at the top surface of the bridge parts when different HT processes are analyzed, respectively. The first sample (as-built) does not go through the annealing HT process and is used as a reference. After cutting from the base plate, this specimen suffers a pronounced deformation, up to 8.2 mm, due to the relaxation of the residual stresses. The rest of the samples experience different HT conditions (see Fig. 6), reducing the component warpage, especially when high temperatures are adopted.

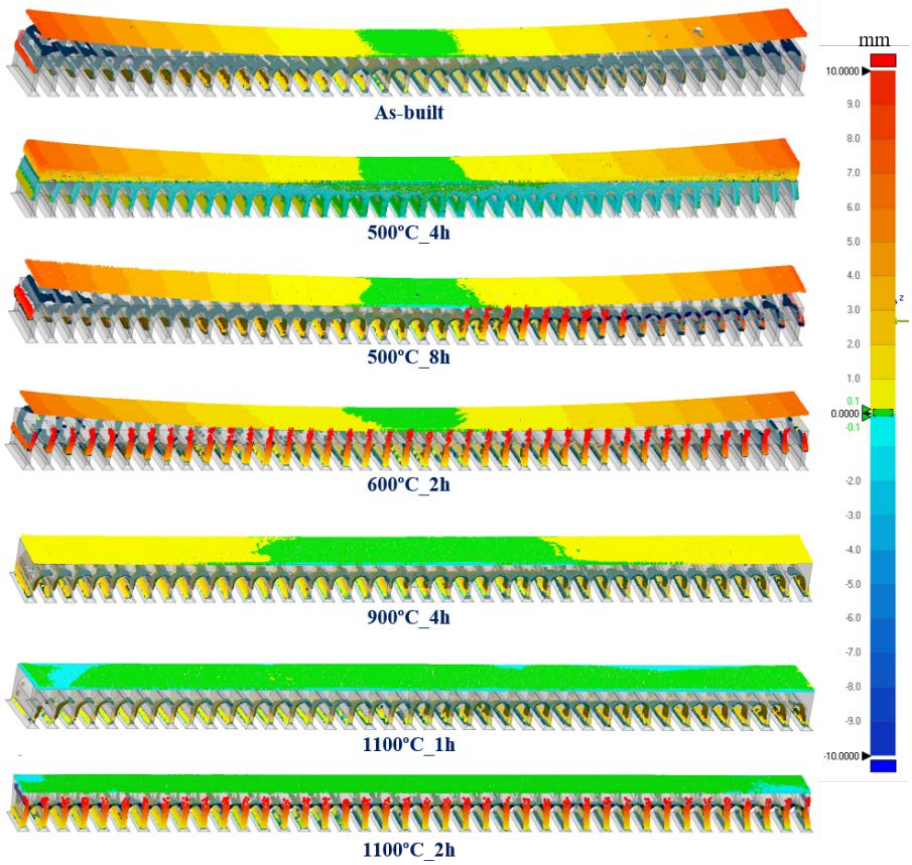

Fig. 6. Contour-fills of the vertical displacements at the top surface of the bridge parts with different annealing HT conditions.

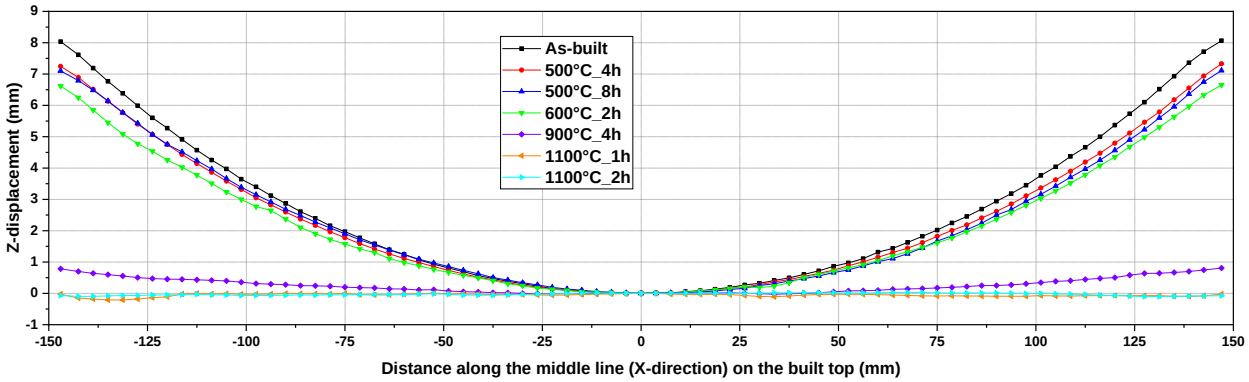

Fig. 7. Vertical displacements along the longitudinal direction at the top surface of the bridge structures after the cutting operation.

The calibration of the proposed numerical model is carried out by the numerical fitting of the experimental measurements, as shown in Fig. 8. In this figure the part-warpages measured by 3D-scanning are compared to the numerical prediction. The agreement between the simulated (red line) and measured (black line) displacements is remarkable.

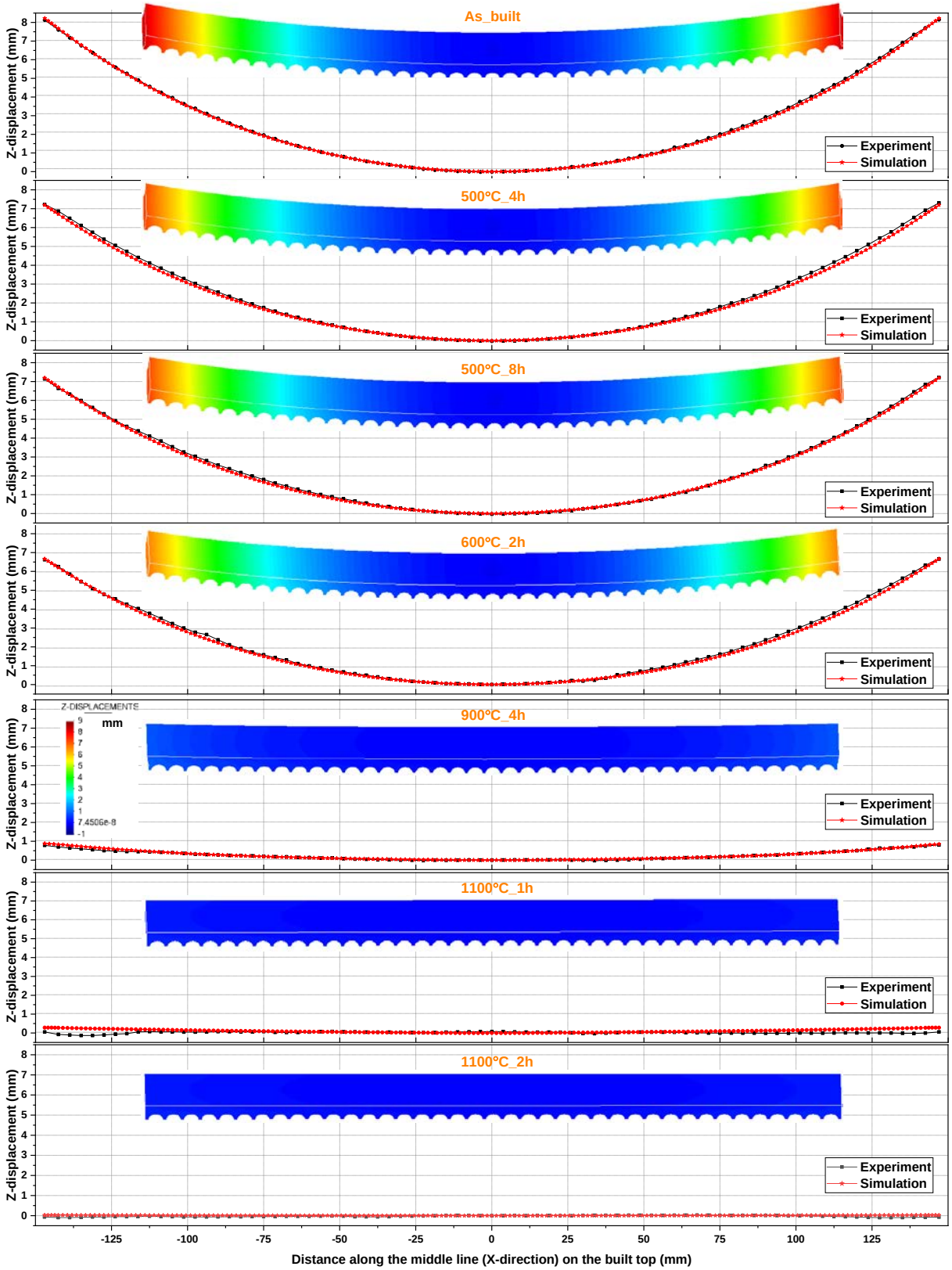

Fig. 8. Comparison between simulated and measured (3D-scanning) warpages along the longitudinal direction at the top surface of the bridge parts.

4.2 Residual stresses after the LPBF and before the HT process

The residual stress field generated by the LPBF before the annealing HT is analyzed in Fig. 9. The longitudinal stresses, σ_{xx}, are reported at different positions along the vertical axis located in the middle of the

bridge part.

The highest temperature experimented during the printing process is approximately 2650°C. After printing, the material quickly solidifies and shrinks. The mechanical constraining due to the previously built layers yields high tensile stresses of about 600 MPa at point A and 900 MPa at points B and C, respectively. The thermal cycles due to the printing process force alternating compressive and tensile longitudinal stresses, gradually reducing their amplitude as the build grows and the thermo-mechanically affected zone moves upward.

When the buildup is completed, the longitudinal residual stress at the lower position (point A) is compressive (-114 MPa) while large tensile stresses occur in the middle (point B) and top (point C) locations of the build of 585 MPa and 941 MPa, respectively. These high residual stresses are released when the bridge part is cut from the base plate as shown in Fig. 9.

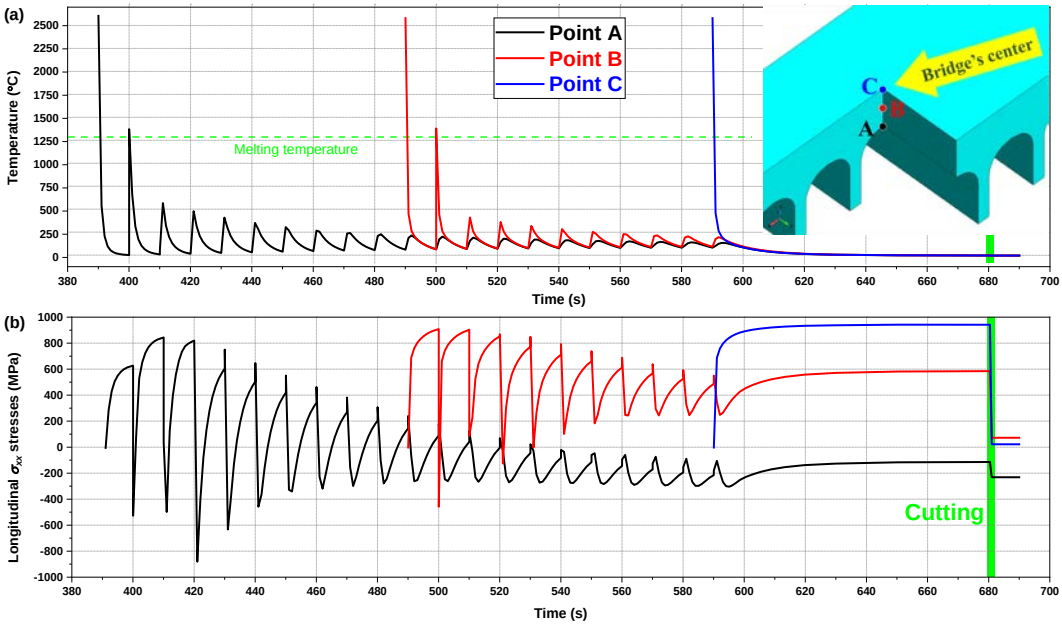

Fig. 9. Evolution of (a) the temperatures and (b) the longitudinal σ_{xx} stresses at different deposition positions in the central section of the bridge part during the LPBF process.

Fig. 10 shows the contour-fills of the residual stresses (equivalent J2 stress) before and after the substrate removal. The large residual stresses (up to 950 MPa) located in the upper part of the AM-built agree with the results reported in previous studies [47,48].

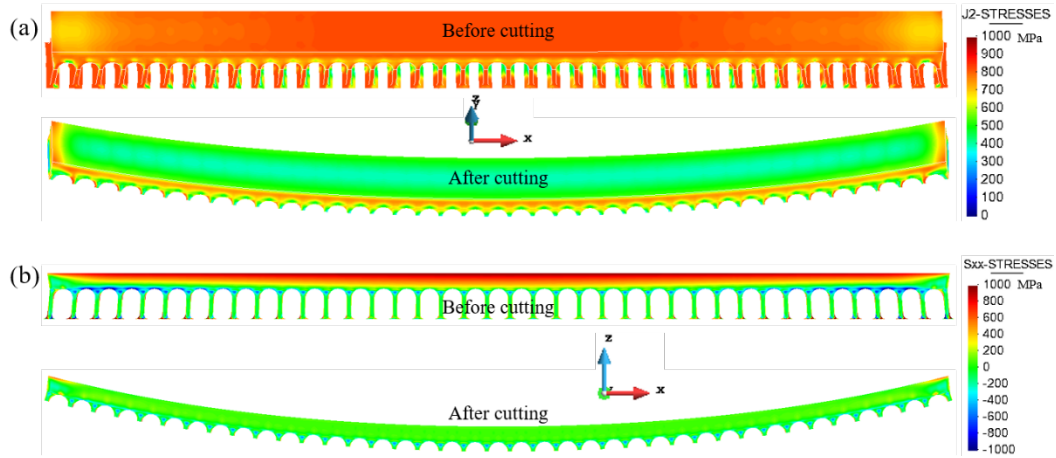

Fig. 10. Comparison of the residual stresses before and after the substrate removal: (a) von Mises stresses of the whole part; (b) longitudinal σ_{xx} stresses at the middle XZ cross-section.

The longitudinal σ_{xx} stress distributions are presented along the longitudinal (L1 and L2) and transversal (L3, L4 and L5) lines as shown in Fig. 11. Lines L1 and L3 are located at the top surface of the built, lines L2 and L4 are located 2.5 mm below the upper surface while line L5 is placed in the lower surface of the upper slab.

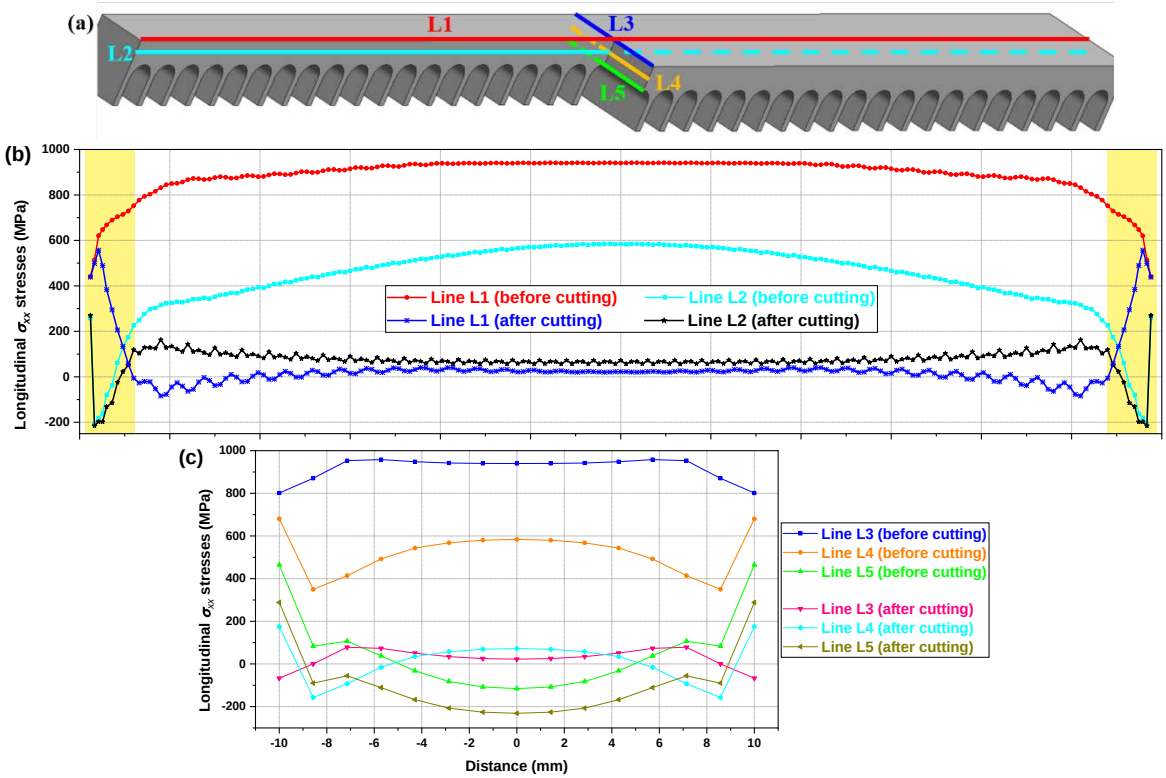

Fig. 11. Longitudinal σ_{xx} stress distributions before and after cutting the supports: (a) Selected locations for the residual stresses analysis; Residual stresses (b) along the longitudinal lines L1 and L2 and, (c) along the transversal lines L3, L4 and L5.

Fig. 12 shows a printing defect at the end of the bridge structure, generally referred to as side loss [49]. The numerical prediction of this geometrical defect is presented in Figure 13, where the contour-fill of the longitudinal (X) displacement is depicted at different stages of the LPBF process. Note that this deformation is quite small (less than 0.1 mm) during the fabrication of the supporting structures. However, during the manufacturing of the upper slab, the resulting shrinkage is gradually amplified by the contraction of each newly deposited layer. As a result, the final side loss is about 0.55 mm. Note that large plastic deformations are generated at both the bridge ends, reducing the residual stresses in these regions as shown by the yellow regions in Fig. 11(b). Fortunately, such side loss defects can be remedied by a geometric compensation solution [12].

Fig. 12. Side loss of the bridge geometry.

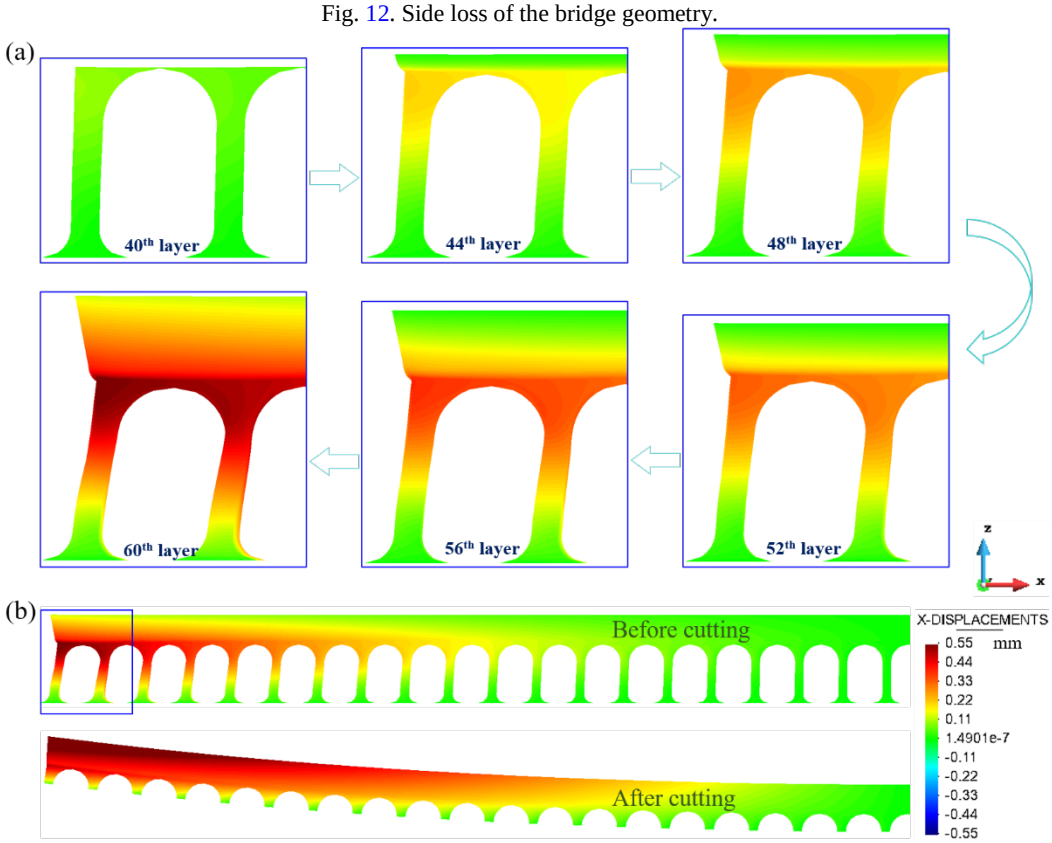

Fig. 13. Longitudinal (X) displacement field: (a) the evolution of the deformed geometry according to the printing process; (b) Part warpage before and after the substrate removal.

4.3 Effect of the annealing parameters on the stress relaxation

The proposed (validated) simulation framework is further used to analyze several post-HT conditions, thus varying both the annealing temperature and the dwell-time. Fig. 14(a) shows the final vertical displacement at the tip end of the bridge parts when using different annealing temperatures in the range from 400 ºC to 1100ºC while fixing the dwell-time to 1 h. It is proven that the final distortion reduces by increasing the annealing temperature. However, the mitigation of the part warpage with respect to the reference (no HT) is quite limited (<20%) for low annealing temperatures (400-600ºC). When the temperature exceeds 900ºC, the annealing effect is evident (>90%) favoring the stress relaxation. During the annealing process, on one hand, the yield stress reduces (thermal softening) as the temperature increases, favoring the creep phenomena. Thus, the visco-plastic strains develop

because of the current stress field. On the other hand, the elasto-visco-plastic model used, when the HT temperature is above the annealing temperature, smoothly transfers into a purely viscous (Norton-Hoff) law where only exclusively viscous (creep) strains can develop.

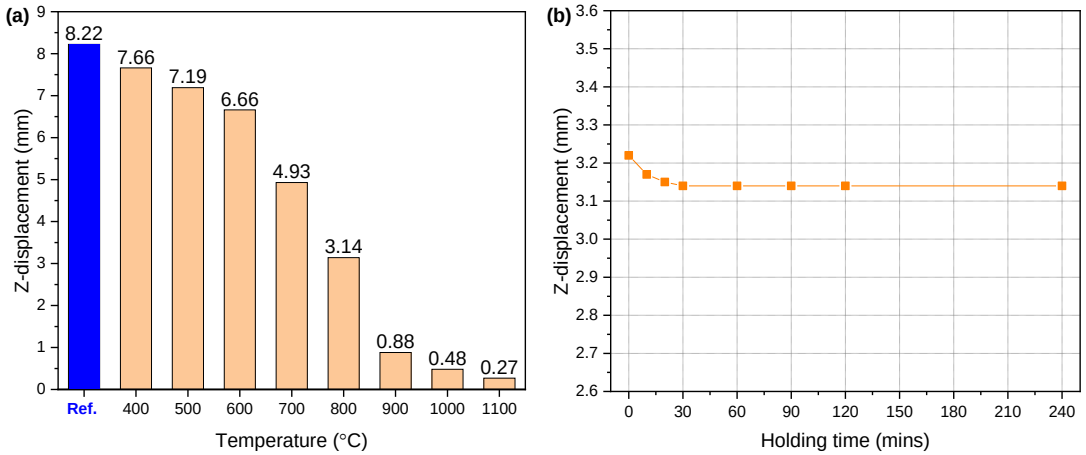

Fig. 14. Vertical (Z) displacement at the end of the bridge component after the support removal: (a) by varying the annealing temperature and assuming a dwell-time of 1 h; (b) by varying the dwell-time at a HT temperature of 800ºC.

Fig. 14(b) shows the vertical displacement at one end of the bridge as a function of the dwell-time for the same annealing temperature of 800ºC. The dwell-time varies between 0 and 240 mins. Note that after the first 30 min of permanence at the annealing temperature, the vertical displacement does not change anymore. On the other hand, just rising the temperature to its final HT value, immediately followed by the component cooling to room temperature has a valuable effect compared to the reference printing which does not consider the HT process. Thus, the annealing temperature is a more sensitive HT parameter for stress release than the dwell-time. A similar result has been reported in [50] for the Ti6Al4V AM process.

Fig. 15 shows the contours of the longitudinal (σ_{xx}) stresses on the central cross-section of the bridge part at different times of the HT process, assuming an annealing temperature of 1100ºC and a dwell-time of 1 h. Note that the initial stress field after the printing process presents large tensile stresses located in the upper slab of the bridge. These stresses gradually reduce during the heating process and almost disappear when the annealing temperature is reached. After a dwell-time of 1 h at 1100ºC, the component is almost stress-free. As a result, a deformation-free part is obtained after removing the supports (see Fig. 8).

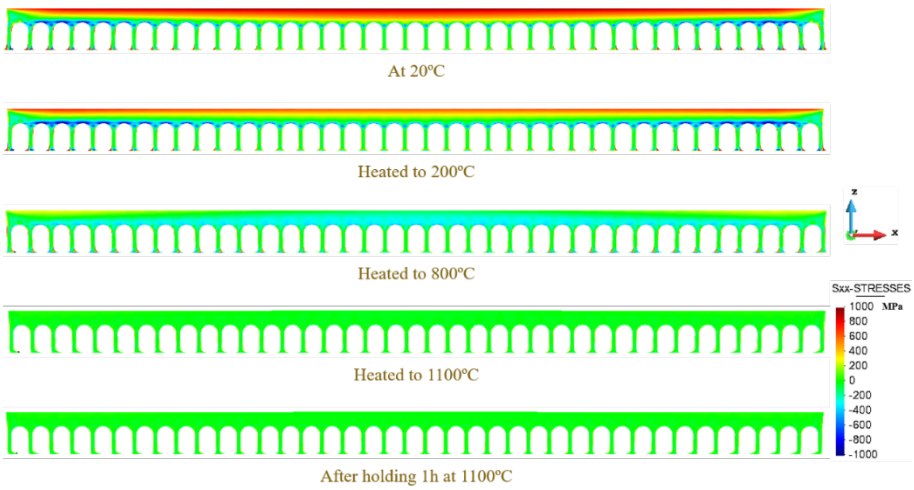

Fig. 15. Evolution of the longitudinal σ_{xx} stresses of the bridge part during the HT annealing of 1100°C_1h.

Collecting all the previous results, it is possible to obtain the optimal process window for post-HT as a function of the annealing conditions. Fig. 16 shows the process-map for the mock-up component in this study, allowing for the quick visualization of the optimal HT parameters.

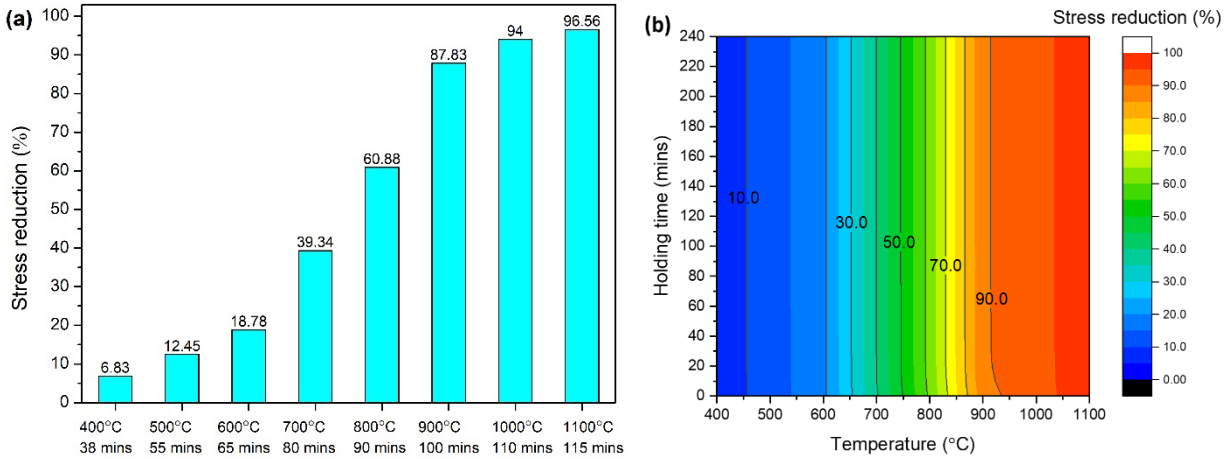

Fig. 16. Process map for post-annealing HT: (a) the stress reduction (%) when the tested parts are just heated to the selected HT temperatures; (b) the effect of the HT temperature and the holding time on the stress reduction.

4.4 Effect of the part size on its mechanical behavior

Depending on the (increasing) dimension of the component, it is necessary to consider longer dwell-time to achieve a stress-free condition [51]. Thereby, in this section, the sensitivity of the annealing process to the slab thickness is investigated, preserving the same length and width. Two new bridge structures defined by increasing the building heights to 22.5 mm and 30 mm are compared to the original one (15 mm high).

Fig. 17(a) shows the side loss, that is, the longitudinal (X) displacement distribution along the vertical line (L6) at the end of the bridge parts. As for the reference geometry, the side loss occurs at the end of the supporting structure where the component exhibits a radical change in its structural stiffness. When increasing the slab thickness, the side loss also increases because of the accumulated thermal shrinkage in these more massive structures.

Fig. 17(b) shows the corresponding longitudinal σ_{xx} stresses along the vertical line (L7) at the center of the bridge structure. The slab is compressed close to the lower surface while tensile stresses arise in the upper part. It is interesting to observe that the magnitude of the tensile stress is similar (about 920 MPa) for all three cases, independently of the slab thickness (printing height). However, the compressive stresses do increase with the thickness due to the number of printed layers.

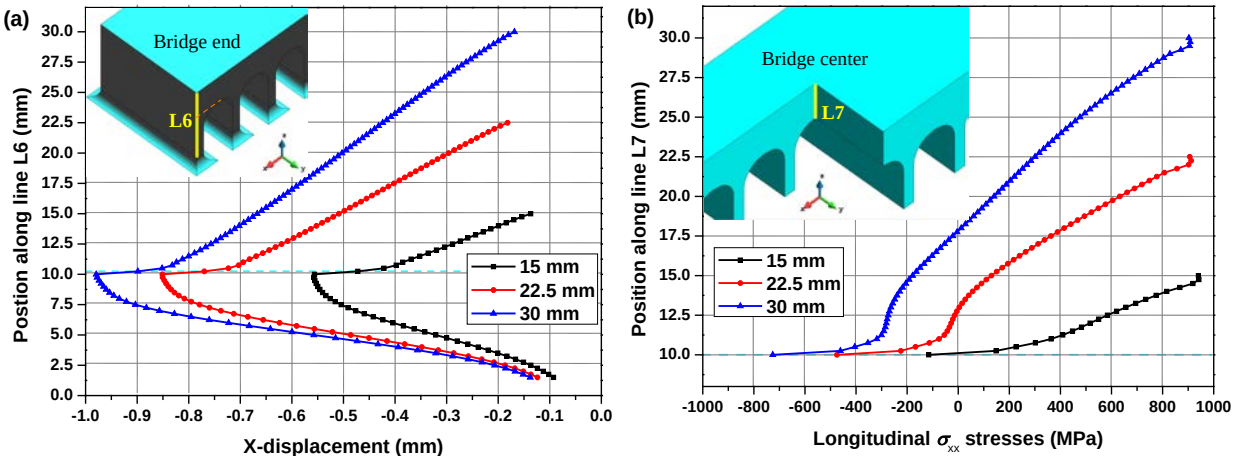

Fig. 17. Three as-built bridge structures with different building heights before HT: (a) X-displacement along line L6 at the end of the build; (b) longitudinal σ_{xx} stresses distribution along line L7 at the center of the build.

Fig. 18 shows the evolution of the longitudinal stress σ_{xx} field of the bridge parts during the LPBF process for increasing building heights from 15 mm to 30 mm. Fig. 19 compares the warpage (vertical displacement) at the top surface of the three bridge parts. It can be observed that the bending reduces from 8.11 mm to 3.16 mm (61% reduction) with the increase of the building height from 15 mm to 30 mm. This is in accordance with the increase of the compressive stresses in the lower part of the slab (see Fig. 18) which restrain the bending of the bridge structure induced by the tensile stresses (with a similar magnitude in all cases) in the upper surface.

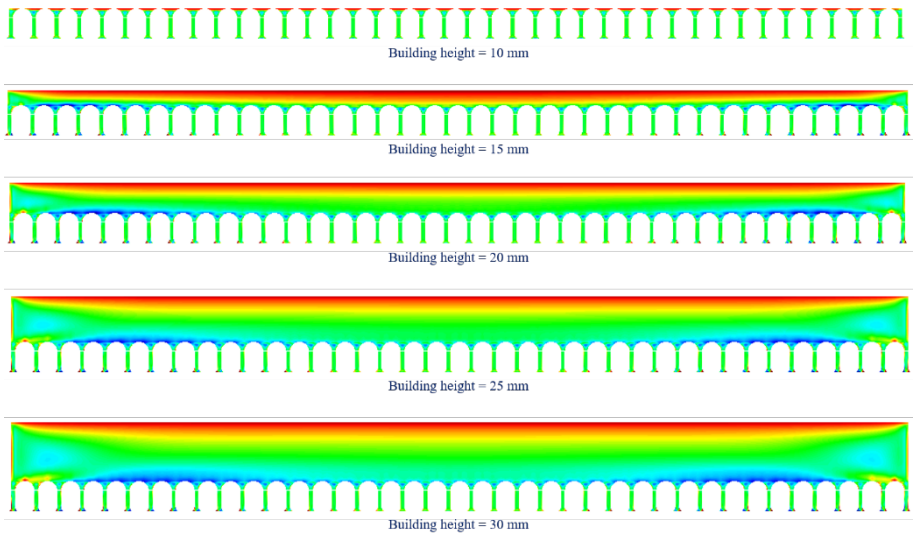

Fig. 18. Evolution of the longitudinal stress σ_{xx} field of the bridge parts during the LPBF process for different building heights from 15 mm to 30 mm.

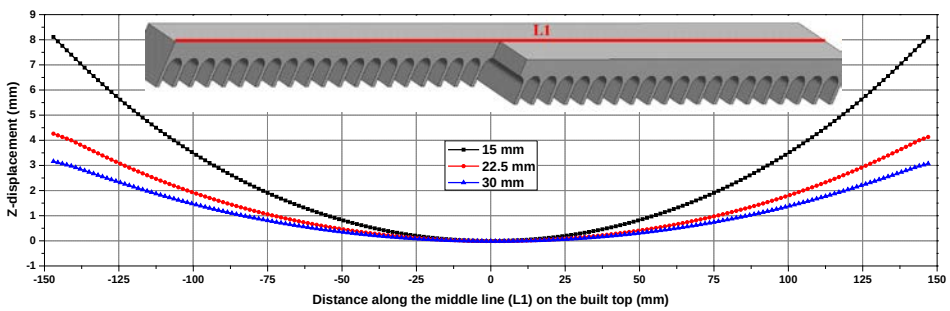

Fig. 19. Vertical displacements on the top of the as-built bridge parts with different building heights after the substrate removal.

To check the potential influence of the part size on stress relief during the annealing process, a post-HT annealing process is numerically performed before cutting the support structures. According to the obtained process-map presented in Fig. 16, an elevated HT temperature of 900°C is chosen for guaranteeing the potent activation of creep while two different holding time (i.e. 0 h and 1 h) are used. Fig. 20 compares the vertical deflections of the three bridge parts after cutting the support structures and the extrapolated stress reduction. Observe that using high-temperature annealing notoriously relieves residual stress and minimizes part warping as expected. Remarkably, the degree of stress relief during the annealing process is more sensitive to the holding time with the increase of the component size. This suggests that a longer holding time is required for the qualification of larger AM-parts.

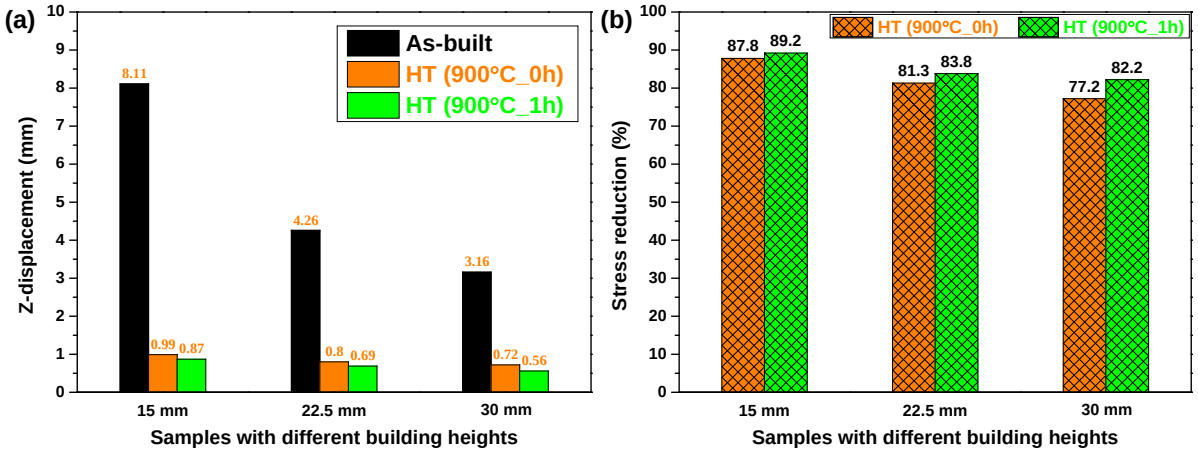

Fig. 20. Mechanical response of the three bridge parts after the HT at 900ºC with two different holding time of 0 h and 1 h: (a) vertical displacements at the tip end of the build after the cutting operation and (b) the corresponding stress reduction.

5 Conclusions

This work establishes a FE computational framework for the thermomechanical simulation of the manufacturing chain including the 3D printing by LPBF, the following annealing HT and the final substrate removal by cutting operation. The main effort to accomplish this objective consists in calibrating the creep model according to the experimental evidence. Therefore, the temperature-dependent visco-plastic evolution laws as well as the thermal softening controlling the evolution of the yield surface are accurately calibrated to characterize the constitutive behavior of the Ni-based GH4099 superalloy.

Next, the developed model is validated by analyzing several annealing HT conditions by varying both the annealing temperature and the dwell-time. The mitigation of the final component warpage and the relaxation of the residual stresses induced by the LPBF process are discussed.

The main findings are:

(1) Once calibrated, the numerical model is able to accurately replicate the entire manufacturing chain with a remarkable agreement with the measured part-warpages, independently of the annealing HT conditions applied and the size of the mock-up component.

(2) The sensitivity analysis carried out by varying the HT parameters shows that the annealing temperature has a more significant impact on stress relief than the dwell-time applied. The stress relaxation begins during the heating phase and when the temperature reaches 1000ºC most of the residual stresses are released in thin

sections. The duration of the necessary dwell-time increases with the size of the components.

(3) A process map for the stress annealing of LPBF-processed GH4099, as shown in Fig. 16, is created by collecting the mechanical results of the multiple annealing conditions analyzed. This process map is useful to select the optimal HT parameters.

6 Acknowledgments

This work was funded by the National Key R&D Programs of China (No. 2022YFB4600300 & No. 2016YFB1100100), the Spanish Ministry of Economy and Competitiveness through the Severo Ochoa Programme for Centers of Excellence in R&D (CEX2018-000797-S) and the China Scholarship Council (No. 201906290011).

7 References

[1] ISO, ASTM. "ISO/ASTM 52900: 2015 Additive Manufacturing–General Principles–Terminology." ASTM F2792-10e1 1 (2015): 1-19.

[2] Gibson, I., D. Rosen, B. Stucker, M. Khorasani, I. Gibson, D. Rosen, B. Stucker, and M. Khorasani. 2021. "Development of additive manufacturing technology." Additive manufacturing technologies 23-51. https://doi.org/10.1007/978-3-030-56127-7_2

[3] Sing, S., and W. Yeong. 2020. "Laser powder bed fusion for metal additive manufacturing: perspectives on recent developments." Virtual and Physical Prototyping 15(3): 359-370. https://doi.org/10.1080/17452759.2020.1779999

[4] Lu, X., W. Zhang, M. Chiumenti, M. Cervera, B. Gillham, P. Yu, S. Yin, X. Lin, R. Babu, and R. Lupoi. 2022. "Crack-free laser powder bed fusion by substrate design." Additive Manufacturing 59: 103149. https://doi.org/10.1016/j.addma.2022.103149

[5] Carraturo, M., S. Kollmannsberger, A. Reali, F. Auricchio, and E. Rank. 2021. "An immersed boundary approach for residual stress evaluation in selective laser melting processes." Additive Manufacturing 46: 102077. https://doi.org/10.1016/j.addma.2021.102077

[6] Zhang, W., M. Tong, and N. Harrison. 2020. "Scanning strategies effect on temperature, residual stress and deformation by multi-laser beam powder bed fusion manufacturing." Additive Manufacturing 36: 101507. https://doi.org/10.1016/j.addma.2020.101507

[7] Setien, I., M. Chiumenti, S. Veen, M. Sebastian, F. Garciandía, and A. Echeverría. 2019. "Empirical methodology to determine inherent strains in additive manufacturing." Computers & Mathematics with Applications 78(7): 2282-2295. https://doi.org/10.1016/j.camwa.2018.05.015

[8] Lu, X., M. Cervera, M. Chiumenti, and X. Lin. 2021. "Residual Stresses Control in Additive Manufacturing." Journal of Manufacturing and Materials Processing 5(4): 138. https://doi.org/10.3390/jmmp5040138

[9] Sanaei, N., and A. Fatemi. 2021. "Defects in additive manufactured metals and their effect on fatigue performance: a state-of-the-art review." Progress in Materials Science 117: 100724. https://doi.org/10.1016/j.pmatsci.2020.100724

[10] Zhang, W., D. Guo, L. Wang, C. Davies, W. Mirihanage, M. Tong, and N. Harrison. 2023. "X-ray diffraction measurements and computational prediction of residual stress mitigation scanning strategies in powder bed fusion additive manufacturing." Additive Manufacturing 61: 103275. https://doi.org/10.1016/j.addma.2022.103275

[11] Promoppatum, P., and S. Yao. 2020. "Influence of scanning length and energy input on residual stress reduction in metal additive manufacturing: Numerical and experimental studies." Journal of Manufacturing Processes 49: 247-259. https://doi.org/10.1016/j.jmapro.2019.11.020

[12] Lu, X., M. Chiumenti, M. Cervera, J. Li, X. Lin, L. Ma, G. Zhang, and E. Liang. 2021. “Substrate Design to Minimize Residual Stresses in Directed Energy Deposition AM Processes.” Materials & Design 202: 109525. https://doi.org/10.1016/j.matdes.2021.109525

[13] Cao, J., M. Gharghouri, and P. Nash. 2016. "Finite-element analysis and experimental validation of thermal residual stress and distortion in electron beam additive manufactured Ti-6Al-4V build plates." Journal of Materials Processing Technology 237: 409-419. https://doi.org/10.1016/j.jmatprotec.2016.06.032

[14] Lu, X., X. Lin, M. Chiumenti, M. Cervera, Y. Hu, X. Ji, L. Ma, H. Yang, and W. Huang. 2019. “Residual Stress and Distortion of Rectangular and S-Shaped Ti-6Al-4V Parts by Directed Energy Deposition: Modelling and Experimental Calibration.” Additive Manufacturing 26: 166–179. https://doi.org/10.1016/j.addma.2019.02.001

[15] Abbaszadeh, M., J. R. Hönnige, F. Martina, L. Neto, N. Kashaev, P. Colegrove, S. Williams, and B. Klusemann. 2019. "Numerical investigation of the effect of rolling on the localized stress and strain induction for wire+ arc additive manufactured structures." Journal of Materials Engineering and Performance 28: 4931-4942. https://doi.org/10.1007/s11665-019-04249-y

[16] Lu, H., J. Lv, K. Luo, and J. Lu. 2022. "Microstructure and Mechanical Properties of Ti6Al4V Alloy by Laser Integrated Additive Manufacturing with Alternately Thermal/Mechanical Effects." Acta Metall Sin 59(1): 125-135. https://www.ams.org.cn/EN/10.11900/0412.1961.2022.00011

[17] Laleh, M., E. Sadeghi, R. Revilla, Q. Chao, N. Haghdadi, A. Hughes, W. Xu, I. Graeve, M. Qian, I. Gibson, and M. Tan. 2022. "Heat treatment for metal additive manufacturing." Progress in Materials Science 133: 101051. https://doi.org/10.1016/j.pmatsci.2022.101051

[18] Croft, D. 1996. "Types of heat treatment" In Heat Treatment of Welded Steel Structures, pp. 9-20. Woodhead Publishing. https://doi.org/10.1533/9781845698812.9
[19] Song, X., S. Feih, W. Zhai, C. Sun, F. Li, R. Maiti, J. Wei, Y. Yang, V. Oancea, L. Brandt, and A. Korsunsky. 2020. "Advances in additive manufacturing process simulation: Residual stresses and distortion predictions in complex metallic components." Materials & design 193: 108779. https://doi.org/10.1016/j.matdes.2020.108779
[20] Lu, X., X. Lin, M. Chiumenti, M. Cervera, J. Li, L. Ma, L. Wei, Y. Hu, and W. Huang. 2018. “Finite Element Analysis and Experimental Validation of the Thermomechanical Behavior in Laser Solid Forming of Ti-6Al-4V.” Additive Manufacturing 21: 30–40. https://doi.org/10.1016/j.addma.2018.02.003
[21] Mugwagwa, L., I. Yadroitsava, N. Makoana, and I. Yadroitsev. 2021. "Residual stress in laser powder bed fusion." In Fundamentals of Laser Powder Bed Fusion of Metals, pp. 245-276. Elsevier. https://doi.org/10.1016/B978-0-12-824090-8.00014-7
[22] Baere, D., P. Cauwenbergh, M. Bayat, S. Mohanty, J. Thorborg, L. Thijs, B. Hooreweder, K. Vanmeensel, and J. Hattel. 2021. "Thermo-mechanical modelling of stress relief heat treatments after laser-based powder bed fusion." Additive Manufacturing 38: 101818. https://doi.org/10.1016/j.addma.2020.101818
[23] Cardon, A., C. Mareau, Y. Ayed, S. Veen, E. Giraud, and P. Santo. 2021. "Heat treatment simulation of Ti-6Al-4V parts produced by selective laser melting." Additive Manufacturing 39: 101766. https://doi.org/10.1016/j.addma.2020.101766
[24] Jin, Q., D. Kang, K. Ha, J. Yu, and W. Lee. 2022. "Simulation of annealing process on AISI 316 L stainless steel fabricated via laser powder bed fusion using finite element method with creep." Additive Manufacturing 60: 103255. https://doi.org/10.1016/j.addma.2022.103255
[25] Williams, R., F. Vecchiato, J. Kelleher, M. Wenman, P. Hooper, and C. Davies. 2020. "Effects of heat treatment on residual stresses in the laser powder bed fusion of 316L stainless steel: Finite element predictions and neutron diffraction measurements." Journal of Manufacturing processes 57: 641-653. https://doi.org/10.1016/j.jmapro.2020.07.023
[26] Li, J., X. Yao, Y. Wang, X. Gao, and Z. Zhang. 2021. "The simulation of post-heat treatment in selective laser melting additive manufacturing." Integrating Materials and Manufacturing Innovation 10: 413-428. https://doi.org/10.1007/s40192-021-00222-7
[27] Hu, Y., X. Lin, Y. Li, J. Wang, S. Zhang, X. Lu, and W. Huang. 2019. "Effect of heat treatment on the microstructural evolution and mechanical properties of GH4099 additive-manufactured by directed energy deposition." Journal of Alloys and Compounds 800: 163-173. https://doi.org/10.1016/j.jallcom.2019.05.348
[28] Chang, K., L. Ma, P. Li, J. Lv, X. You, Y. Zhang, and Y. Tan. 2023. "Effect of heat treatment on microstructure and mechanical properties of GH4099 superalloy fabricated by selective laser melting." Journal of Alloys and Compounds 934: 167813. https://doi.org/10.1016/j.jallcom.2022.167813
[29] Mostafaei, A., R. Ghiaasiaan, I. Ho, S. Strayer, K. Chang, N. Shamsaei, S. Shao, S. Paul, A. Yeh, S. Tin, A. To. 2023. "Additive Manufacturing of Nickel-based superalloys: a state-of-the-art review on process-structure-defect-property relationship." Progress in Materials Science 101108. https://doi.org/10.1016/j.pmatsci.2023.101108
[30] Hu, Y., X. Lin, S. Zhang, Y. Jiang, X. Lu, H. Yang, and W. Huang. 2018. "Effect of solution heat treatment on the microstructure and mechanical properties of Inconel 625 superalloy fabricated by laser solid forming." Journal of Alloys and Compounds 767 (): 330-344. https://doi.org/10.1016/j.jallcom.2018.07.087
[31] Lu, X., G. Zhang, J. Li, M. Cervera, M. Chiumenti, J. Chen, X. Lin, and W. Huang. 2021. "Simulation-assisted investigation on the formation of layer bands and the microstructural evolution in directed energy deposition of Ti6Al4V blocks." Virtual and Physical Prototyping: 1-17. https://doi.org/10.1080/17452759.2021.1942077
[32] Chiumenti, M., M. Cervera, N. Dialami, B. Wu, L. Jinwei, and C. Saracibar. 2016. "Numerical modeling of the electron beam welding and its experimental validation." Finite Elements in Analysis and Design 121: 118-133. https://doi.org/10.1016/j.finel.2016.07.003
[33] Lu, X., M. Chiumenti, M. Cervera, G. Zhang, and X. Lin. "Mitigation of residual stresses and microstructure homogenization in directed energy deposition processes." Engineering with Computers (2022): 1-20. https://doi.org/10.1007/s00366-021-01563-9
[34] Chiumenti, M., M. Cervera, A. Salmi, C. A. Saracibar, N. Dialami, and K. Matsui. 2010. "Finite element modeling of multi-pass welding and shaped metal deposition processes." Computer methods in applied mechanics and engineering 199(37-40): 2343-2359. https://doi.org/10.1016/j.cma.2010.02.018
[35] Chen, Q., X. Liang, D. Hayduke, J. Liu, L. Cheng, J. Oskin, R. Whitmore, and A. To. 2019. "An inherent strain based multiscale modeling framework for simulating part-scale residual deformation for direct metal laser sintering." Additive Manufacturing 28: 406-418. https://doi.org/10.1016/j.addma.2019.05.021
[36] An, K., L. Yuan, L. Dial, I. Spinelli, A. Stoica, and Y. Gao. 2017. "Neutron residual stress measurement and numerical modeling in a curved thin-walled structure by laser powder bed fusion additive manufacturing." Materials & design 135: 122-132. https://doi.org/10.1016/j.matdes.2017.09.018
[37] Lu, X., X. Lin, M. Chiumenti, M. Cervera, Y. Hu, X. Ji, L. Ma, and W. Huang. 2019. “In Situ Measurements and ThermoMechanical Simulation of Ti-6Al-4V Laser Solid Forming Processes.” International Journal of Mechanical Sciences 153-154: 119–130. https://doi.org/10.1016/j.ijmecsci.2019.01.043
[38] Chiumenti, M., M. Cervera, C. Saracibar, and N. Dialami. 2013. "Numerical modeling of friction stir welding processes." Computer methods in applied mechanics and engineering 254: 353-369. https://doi.org/10.1016/j.cma.2012.09.013
[39] Wang, S., S. Tao, and H. Peng. 2022. "Influence of powder characteristics on the microstructure and mechanical behaviour of GH4099 superalloy fabricated by electron beam melting." Metals 12(8): 1301. https://doi.org/10.3390/met12081301
[40] China Aeronautical Materials Handbook Editorial Committee. 2011. China Aeronautical Materials Handbook: Deformed Superalloys, Cast Superalloys [M]. Beijing: China Standard Press, 278-293.
[41] Lu, Z., C. Zhang, N. Deng, H. Zhou, R. Fang, K. Gao, Y. Su, and H. Zhang. 2022. "Influence of selective laser melting process parameters on microstructure and properties of a typical Ni-based superalloy." Acta Metallurgica Sinica (English Letters) 35(10): 1673-1687. https://doi.org/10.1007/s40195-022-01401-x
[42] Khorasani, M., A. Ghasemi, M. Leary, E. Sharabian, L. Cordova, I. Gibson, D. Downing, S. Bateman, M. Brandt, and B. Rolfe. 2022. "The effect of absorption ratio on meltpool features in laser-based powder bed fusion of IN718." Optics & Laser

Technology 153: 108263. https://doi.org/10.1016/j.optlastec.2022.108263
[43] Shahabad, S., Z. Zhang, A. Keshavarzkermani, U. Ali, Y. Mahmoodkhani, R. Esmaeilizadeh, A. Bonakdar, and E. Toyserkani. 2020. "Heat source model calibration for thermal analysis of laser powder-bed fusion." The International Journal of Advanced Manufacturing Technology 106: 3367-3379. https://doi.org/10.1007/s00170-019-04908-3
[44] Denlinger, E., M. Gouge, J. Irwin, and P. Michaleris. 2017. "Thermomechanical model development and in situ experimental validation of the Laser Powder-Bed Fusion process." Additive Manufacturing 16: 73-80. https://doi.org/10.1016/j.addma.2017.05.001
[45] Denlinger, E., V. Jagdale, G. Srinivasan, T. El-Wardany, and P. Michaleris. 2016. "Thermal modeling of Inconel 718 processed with powder bed fusion and experimental validation using in situ measurements." Additive Manufacturing 11: 7-15. https://doi.org/10.1016/j.addma.2016.03.003
[46] Promoppatum, P., and V. Uthaisangsuk. 2021. "Part scale estimation of residual stress development in laser powder bed fusion additive manufacturing of Inconel 718." Finite Elements in Analysis and Design 189: 103528. https://doi.org/10.1016/j.finel.2021.103528
[47] Liang, X., W. Dong, Q. Chen, and A. To. 2021. "On incorporating scanning strategy effects into the modified inherent strain modeling framework for laser powder bed fusion." Additive Manufacturing 37: 101648. https://doi.org/10.1016/j.addma.2020.101648
[48] Xie, D., F. Lv, H. Liang, L. Shen, Z. Tian, J. Zhao, Y. Song, and C. Shuai. 2021. "Towards a comprehensive understanding of distortion in additive manufacturing based on assumption of constraining force." Virtual and Physical Prototyping 16(1): S85-S97. https://doi.org/10.1080/17452759.2021.1881873
[49] Ghaoui, S., Y. Ledoux, F. Vignat, M. Museau, T. Vo, F. Villeneuve, and A. Ballu. 2020. "Analysis of geometrical defects in overhang fabrications in electron beam melting based on thermomechanical simulations and experimental validations." Additive Manufacturing 36: 101557. https://doi.org/10.1016/j.addma.2020.101557
[50] Wang, Z., A. Stoica, D. Ma, and A. Beese. 2017. "Stress relaxation behavior and mechanisms in Ti-6Al-4V determined via in situ neutron diffraction: Application to additive manufacturing." Materials Science and Engineering: A 707: 585-592. https://doi.org/10.1016/j.msea.2017.09.071
[51] Rajan, T., C. Sharma, and A. Sharma. 2011. "Heat Treatment Processes for Steels" Heat treatment: principles and techniques, Second Edition, pp. 86-91. PHI Learning Pvt. Ltd.